Article

Super-Resolution without Imaging: Library-Based Approaches Using Near-to-Far-Field Transduction by a Nanophotonic Structure

Robin D. Buijs, Nick J. Schilder, Tom A. W. Wolterink, Giampiero Gerini, Ewold Verhagen, and A. Femius Koenderink*

Cite This: *ACS Photonics* 2020, 7, 3246−3256

Read Online

ACCESS | Metrics & More | Article Recommendations

ABSTRACT: Super-resolution imaging is often viewed in terms of engineering narrow point spread functions, but nanoscale optical metrology can be performed without real-space imaging altogether. In this paper, we investigate how partial knowledge of scattering nanostructures enables extraction of nanoscale spatial information from far-field radiation patterns. We use principal component analysis to find patterns in calibration data and use these patterns to retrieve the position of a point source of light. In an experimental realization using angle-resolved cathodoluminescence, we retrieve the light source position with an average error below $\lambda/100$. The patterns found by principal component analysis reflect the underlying scattering physics and reveal the role the scattering nanostructure plays in localization success. The technique described here is highly general and can be applied to gain insight into and perform subdiffractive parameter retrieval in various applications.

KEYWORDS: *super-resolution, metrology, optical sensing, nanostructure, cathodoluminescence, plasmonic antennas*
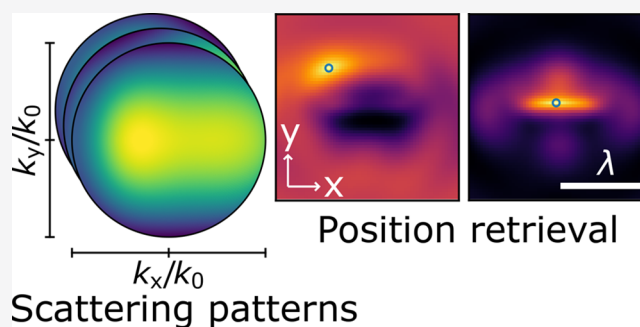
Advances in semiconductor technology and the biological sciences generate great interest in optical characterization at nanometer scales. Because wide-field microscopy is fundamentally unable to reproduce nanometer-scale details, due to the diffraction limit,[1] a wide range of super-resolution techniques, which work around this diffraction limit, have been developed and deployed.[2,3] These techniques are used in direct imaging as well as in precision metrology, which relies on many of the same phenomena.[4,5] Many super-resolution techniques rely on exploitation of a carefully engineered point spread function (PSF) that describes the transformation from a point on the sample to the image plane. In the case of fluorescent super-resolution techniques, like photoactivated localization microscopy (PALM),[6−8] an image is built up by individually identifying and localizing optically active sites by fitting their PSF, which requires precise knowledge of the PSF and invokes the assumption that the active sites are sparse point emitters. In contrast, near-field scanning optical microscopy (NSOM)[9−11] achieves high-fidelity images by constructing a maximally sharp PSF, at the cost of a complicated measurement apparatus. Techniques using a PSF either require explicit inversion through computational elimination of the PSF from image features, or produce an image that is smoothed out by convolution with the PSF. In both cases, spatial resolution scales with PSF width and a good PSF model is crucial to the success of the technique.

Looking beyond the paradigms of real-space imaging, it is very well possible to circumvent the need for a PSF model and retrieve spatial information from radiation patterns directly. The scattering properties of nanophotonic structures depend strongly on their nanoscale features, with parameters such as relative position, size, and permittivity of features all affecting far-field information channels, such as radiation pattern, scattering spectrum, and total radiative rate. Such changes in scattered signals may be observed, regardless of the details of the imaging system. Figure 1 sketches the particular case where a light source moves in the vicinity of an optical antenna. This displacement leads to clear changes in the radiation pattern (scattered intensity vs direction) as a function of displacement, illustrating the principle that the structure factor of a scattering system provides information about its internal configuration. This insight has already enabled nanoscale information retrieval in particle detection,[12,13] position sensing,[14−16] and even imaging.[17−19] Propagation of spatial information through strongly scattering systems has also been studied in the context
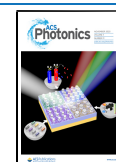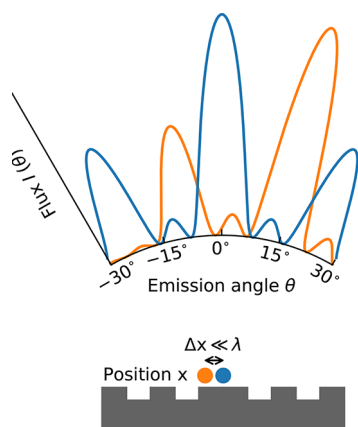
Figure 1. Nanoscale changes in system parameters can strongly modify far-field scattering behavior. Here, a shift in scattering patterns reveals the small displacement of a light source with respect to a scattering structure.

of imaging through complex media.[20−23] However, the general challenge of imaging-free retrieval of nanoscopic information remains largely unexplored.

In this work, we study how a scattering structure in the near-field of a sample embeds nanoscopic information into far-field radiation patterns, enabling the experimental retrieval of the position of a point-like source of light with deeply subwavelength precision. In doing so, we introduce a general-purpose localization technique based on principal component analysis, which provides understanding of which features in radiation patterns contribute to localization precision. We verify that this precision is indeed caused by the scattering structure through comparison with dummy measurements. More generally, we discuss how information about specific features of partially known systems may be extracted from alternative far-field channels, such as radiation

patterns, rather than from real-space imaging of parts of a sample.

PARAMETER RETRIEVAL METHOD

To demonstrate our parameter retrieval procedure, we first discuss a synthetic experiment on the basis of a theoretical toy model. This model consists of a point source of light located in a plane that lies a fraction of a wavelength below a subdiffractive linear array of four scattering sites, as shown schematically in Figure 2a. We consider strong scatterers with parameters such as we might find for the plasmonic resonance of silver nanoparticles 100 nm in diameter.[24] Our objective is to retrieve the position of the light source with respect to the array, just from far-field scattering patterns. We describe this system with a discrete dipole model. This powerful tool to study the qualitative behavior of collections of scattering sites[25−28] natively includes multiple scattering, self-action, and propagation delay.[29,30] Multiple scattering leads to induced dipole moments for each of the array antennas, depending on light source position. Variations in the far-field scattering patterns then result from interference between the different scattering pathways. Figure 2b,c shows calculated scattering patterns for two positions of the light source, plotted as radiant flux as a function of parallel momentum into the upper half-space above the structure and source. The parallel momentum $k_x = k_0 \cos \phi \sin \theta$ and $k_y = k_0 \sin \phi \sin \theta$ is equivalent to a reporting of azimuthal angle ϕ and polar angle θ (angle relative to the normal to the scattering target), and this type of scattering pattern is readily measured in nanophotonics, for instance, through back-focal plane detection.[31−33] In the present example, the radiation pattern has only a comparatively broad feature due to the small spatial extent of the target (Figure 2b). The pattern shifts and changes upon a change of source position (compare Figure 2b and c). A set of such scattering patterns for light source positions spaced $\lambda/32$ apart,
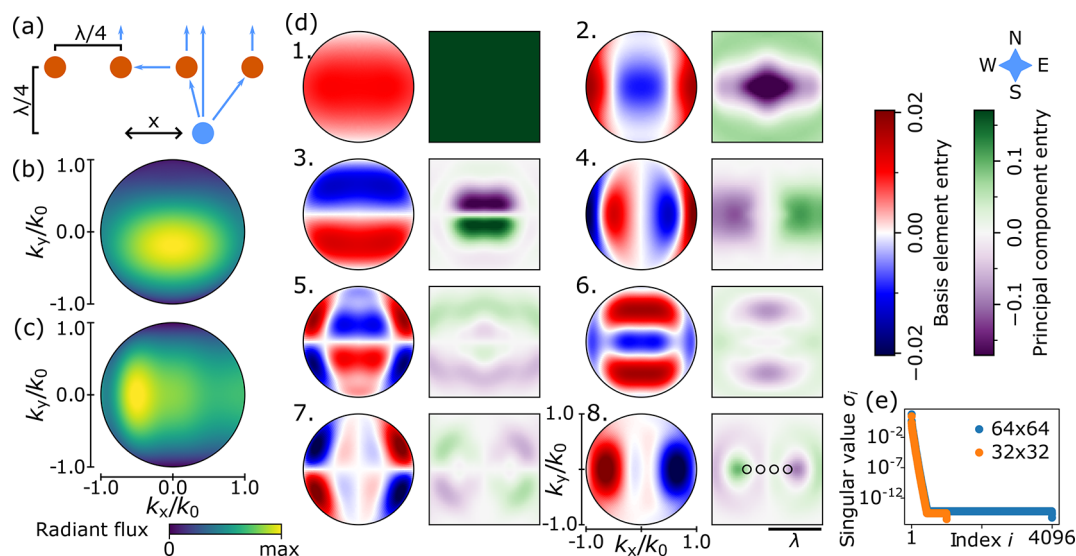

Figure 2. Library-based parameter retrieval from synthetic far-field scattering patterns. (a) Layout of the scattering problem: a light source moves with respect to a four-element chain of scatterers. (b) Calculated scattering pattern for the light source 0.25λ south of the center of the array. (c) Scattering pattern for a light source 0.90λ east of center. (d) Singular value decomposition of a set of reference radiation patterns. Round panels show radiation pattern basis elements versus wavevector and square panels show principal components versus reference position. Numbers indicate the index of the element, as ordered by singular value. Black circles indicate the position of the array elements. (e) Singular values for the decomposition in (d) and for the same problem at half the spatial resolution.

in a 64×64 grid, constitutes a library of synthetic reference data.

In order to systematically identify patterns in the library, we employ the technique of principal component analysis (PCA), which is used in a variety of fields to help detect patterns in complicated data sets.[34−36] Specifically, we construct a matrix A whose rows contain the pixel intensities for each of the normalized reference images A_i. Reference images are Euclidian normalized to $\|A_i\| = 1$ to help us study patterns without strong effects from intensity variations. Singular value decomposition (SVD) allows any matrix A to be rewritten as $A = U\Sigma V^*$, where the asterisk represents conjugate transposition, with U and V unitary matrices and Σ diagonal.[37] For mathematical convenience, we will work only with libraries that have more pixels per image than images in the library, so that Σ has one entry per reference image. The entries of Σ are the singular values σ_i of the set of images A and represent the weight that each basis element has in the original data set. For every singular value, the corresponding column of V forms an optimal basis vector, or basis element, and the corresponding column of U presents its overlap with each of the reference images in the data set A. It is instructive to consider $U\Sigma$ as a single unit, known as the principal components of the data set A. The basis elements are defined in the same coordinate space as the reference images, meaning that they cover a circular domain in (k_x, k_y)-space. The principal components form maps on the same spatial coordinate grid as the reference positions. Together, they describe the basis that most efficiently reproduce the reference data set. In particular, when ranked by singular value, the first basis element has the largest possible overlap with all reference images. Every next basis element has the largest possible overlap with the part of the reference images that is orthogonal to all previous basis elements. PCA thus provides a highly efficient way to encode arbitrary data sets in terms of shared features in their entries.

We now take the SVD of our synthetic reference library in order to investigate what shared features the decomposition identifies. Part of this SVD is shown in Figure 2d. For each component, we show the basis element of the angle-dependent scattered far-field (left, circular maps, red-white-blue color-scale) and the corresponding principal components as a function of light source position in a plane (right, square maps, green-purple scale). Each set of principal components shows the degree to which the corresponding basis element contributes to the total scattering signal at each position. The complete basis has $64^2 = 4096$ such pairs, one per image in the reference library, of which we show only those few with the largest principal components. The first basis element has a large positive value for all wave vectors, and its corresponding principal component map shows that it is almost uniformly high at all reference positions. This element thus corresponds to the common features shared by all radiation patterns. Further elements have a more intricate structure and, moreover, present principal components that are position-dependent. In other words, these higher-order elements quantify the degrees of freedom in the radiation patterns in the library that form the main variation, and the principal components quantify how strongly these elements admix into the response as a function of the source position. In linear algebra terms, each given reference image in the library can be decomposed in the basis elements, with expansion coefficients varying exactly as the principal components with source position. The principal component maps thus provide direct

information on the position at which any given reference image was taken. Focusing on a salient feature as an example, basis elements such as the third show beaming by the array, where moving the light source along the north−south axis (as per the compass in Figure 2) concentrates light emission in that direction, in line with the literature on plasmonic phased arrays.[38−40] This is also seen in the radiation pattern in Figure 2b, which corresponds to a position near the maximum of the third set of principal components. As another example, the left and right end points of the array (along the east−west axis in the principal component images) appear as special points, at which the sets of principal components vary sharply, particularly visible in the fourth and eighth sets of principal components. We see the westward band of the fourth set of principal components in the radiation pattern in Figure 2c, corresponding to a position near the eastern edge of the principal component maps. These examples show that PCA can provide an effective summary of the physical response of a complex scattering problem, decomposed into a small set of physically intuitive contributors.

Basis elements and their principal components are seen to have the broadest features for the largest principal components. This matches the interpretation that the largest principal components correspond to the dominant, most general, features in radiation patterns. In contrast, the lowest-weight elements (not shown) largely encode numerical details and noise that is orthogonal between reference images. The smooth features of the basis elements show us that the fine angular resolution used in these calculations is not required to recognize the important features. The fact that some, like the seventh and eighth basis elements, rely on specific features at large angles suggests that the large numerical aperture used is of particular value. As a rule of thumb, the physical size of a transducer ultimately determines the multipole moments that it supports and that radiate into the far-field, which in turn determines the angular span over which radiation pattern variations occur. The information relevant for position retrieval is contained in the few basis elements with the largest singular values. Indeed, we see in Figure 2d that the later pairs are characterized by a much finer structure in both the basis element and the principal components. PCA of calibration data reveals that only a few features in radiation patterns carry a lot of weight in explaining the full data set. This indicates that most of the basis can be discarded with little loss of information, allowing efficient storage of the library and affirming that the SVD has identified a small number of important radiation pattern features. An excellent question is how many basis elements (and corresponding principal components) are required to encode the variability in radiation patterns. While mathematically the dimensionality increases with spatial sampling density, in reality the basis elements and their weight in the decomposition are set by the scattering physics. Indeed, simulations with lower sampling density yield the same dominant basis elements and a similar drop off of the magnitude of the singular value with index, as seen in Figure 2e. Basis functions lose physical significance once their singular value hits a noise floor set by numerical or experimental noise, around index 400 in this example. For a given numerical, synthetic, or experimental noise level, the number of relevant basis elements is given by the rate of the singular value drop-off versus index.

In order to use the library for parameter retrieval, we take a radiation pattern for any light source position within the

sampled domain and project it onto the optimal basis in the library. The coefficients of this projection are to be compared to the principal components for each reference image. In case the sample radiation pattern is identical to one of the library radiation patterns, there will be a perfect match with the principal components at the corresponding position. More generally, the projection coefficients for any sample radiation pattern form a coordinate vector in a higher dimensional space, in which each of the reference images also has a coordinate, given by their principal components. The best match between sample image and library image can then be obtained by finding the library coordinates that have minimum Euclidean distance to the sample coordinate. This best matching image would then pinpoint the sample image source positions. Quantitatively, in order to produce a match in the range $[0, 1]$, matches between a set of principal components $(U\Sigma)_j$ and a sample image S_i normalized to $\|S_i\| = 1$ are calculated as

$$M_{ij} = 1 - \frac{1}{\sqrt{2}} \left\| (U\Sigma)_j - S_i V \right\| \qquad (1)$$

Such an analysis can be seen in Figure 3a, where the projection match with each reference position is shown for three sample positions (indicated by circles). For now we do not consider distortions or noise, so the radiation patterns used here are identical to reference data at the same positions. Matches at the correct positions are perfect and there is no ambiguity in the choice of best estimate. Overall, positions closer to the correct position are more similar to the sample data than those farther away, while the precise contours echo the principal components of the reference data set. The first panel of Figure 3a, in a corner of the calibrated region, is a fairly good match, with most positions far away from the array due to principal components that peak sharply around the array. Conversely, the third panel matches fairly well only with positions close to the array. In all three cases, the specific structure of principal components around the sampled positions allows unambiguous position retrieval.

To maximize robustness to noise, the projection match should peak as sharply as possible. Peak sharpness can thus be taken as a measure of localization confidence in noisy systems. We quantify this confidence by defining a viability threshold Θ: points significantly above the median match in the projection maps are considered viable solutions, by $\Theta = \eta \max(M) + (1 - \eta) \operatorname{median}(M)$, where M values are the match values between a given scattering pattern and each library entry. Practically, we use a viability criterion $\eta = 1 - 1/e \approx 63\%$, in line with the common definitions of line width. With this threshold, we find the number of points larger than the threshold N_v and define the confidence interval W as the full-width of a symmetric peak of equal area,

$$W = \sqrt{\frac{4}{\pi}} \Delta r \sqrt{N_v} \qquad (2)$$

where Δr is the library sampling step size. This measure of confidence, shown in Figure 3b, generally behaves as we would expect: it is maximal at the ends of the array and low far away from it. The finest confidence intervals are found where the library's principal components (Figure 2d) have the largest gradients, like in the position indicated in the middle panel of Figure 3a, where both the second and the third sets of principal components are strongly position-dependent; conversely, no principal components vary strongly just north and south of the
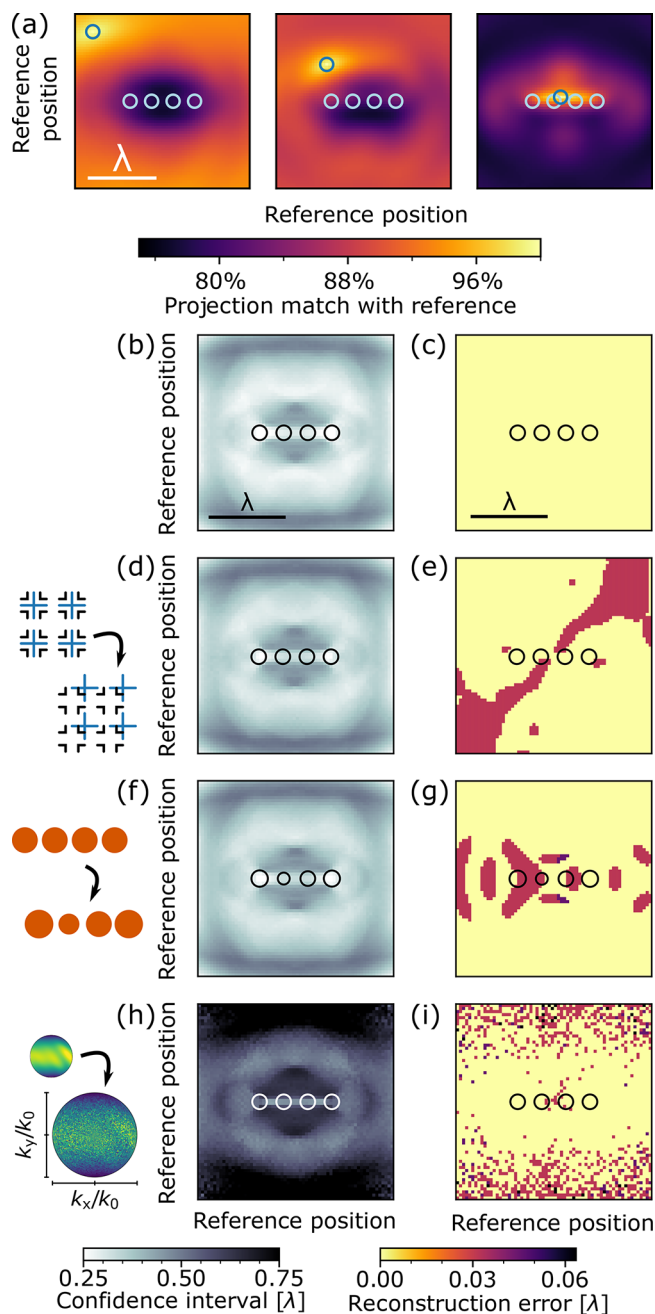

Figure 3. Position retrieval using a library. (a) Match between library and ideal data vs reference position for three different light source positions, marked with blue circles. White circles indicate array element positions. (b−i) Localization confidence interval and sample position reconstruction error vs reference position for four types of data. (b, c) Ideal data. (d, e) Sample positions displaced 30% of a library step to the north and east with respect to library positions. (f, g) Sample data taken with array elements randomly changed in diameter by up to 5%. Circles sized proportionally to element scattering strength. (h, i) Sample data degraded by shot noise as for a signal with an average of three counts per pixel, as shown to the left of (h).

array, leading to low confidence in those regions. Confidence also peaks in the corners of the reference region, as an artifact resulting from the relative rarity of neighbors. Features seen in the confidence map are robust to the precise value of η, remaining similar all the way from $\eta = 50\%$ to 80%. This allows the confidence intervals to be used to evaluate how sensitively

a given transducer lets us retrieve position, or parameters more broadly, in different regions.

In our demonstration so far, we have used the same synthetic data for calibration and testing. This leads to correct retrieval of all positions, as seen in Figure 3c, where the distance between known sample position and best estimate based on library comparison is shown versus reference position. In practical use, we expect various nonidealities. Sample data may be taken at slightly different positions than reference data, the transducer may be different between reference and sample measurements and signals may be noisy. We will study the effects of each of these distortions in our theoretical model. First, we consider position retrieval with sample data taken on a grid of positions displaced by 30% of the step size ($\lambda/32$) to the north and east with respect to the reference grid and project these onto the original library. Projection matches are visually indistinguishable from the data in Figure 3a, as they should be: the projection matches are smooth and the confidence map shows a feature size of roughly $\lambda/2$, so a step of under $\lambda/32$ should not make much of a difference. Localization confidence itself is affected slightly, as seen in Figure 3d, which we attribute to the shift in position causing a slight broadening of the projection match peaks. Though each sample position still has a clear nearest reference position, the best estimate does not always find this position, as seen in Figure 3e. As the principal component landscape is not flat, one of the three other surrounding reference positions may indeed provide a better match than the nearest reference position. Where the nearest position is not the best match, the best match is found either one step east or one step north in every case, supporting this interpretation. In experiment, noise may make it more likely that a further-off point provides the best match. In the low-noise regime, symmetry may still be broken by numeric artifacts in the low-weight basis elements. We also note that much larger sample positioning errors would bring the new sample positions closer to other reference positions, which would lead to reliable localization with a fixed offset, so that the current scenario should be considered the worst case for this type of error. The second type of nonideality concerns our assumption that the transducer does not change. In practice, it may be desirable to use calibration for one device to perform parameter retrieval with another, despite minor fabrication imperfections. Any single transducer may also degrade over time. To judge the effect of such changes, we calculate sample data using the original reference positions, but changing the effective diameter of each array element by a random amount up to 5%, as might occur in a lithography process. We apply our parameter retrieval procedure, again using the original library. As for the shifted sampling grid, projection matches are visually indistinguishable from those Figure 3a, but localization confidence intervals (Figure 3d) broaden slightly, similar to the shifted case. Best match positions are off in a number of places, but errors are under two steps ($\lambda/16$) everywhere. Finally, we explore the effect of noise. We calculate radiation patterns affected by shot noise as for an average signal level of 3 counts per pixel over our 181×91 pixel detector. We attempt position retrieval using the original library. Confidence intervals (Figure 3h) are much broader than for the other cases as the noise makes library match worse for all positions. Despite the high noise level, the vast majority of positions are retrieved correctly and errors of two steps or more are rare. Most errors occur near the north and south ends of the reference area, far from the array,

where confidence intervals are broadest. The scenarios explored here represent a wide range of experimental imperfections. Each shows limited impact on localization success. This makes us confident that the parameter retrieval technique will prove robust to the differences between different experimental realizations.

The success of this theoretical demonstration allows us to reflect on the main merits of our approach, as opposed to other possible approaches that retrieve position information from far-field scattering patterns. In particular, our proposed method envisions a library-based retrieval that applies PCA to real-world calibration data, in other words, proposing a matching of measured data to a previously measured library. This should be juxtaposed to model-based/model-assisted approaches. Scattering properties of complex nanophotonic structures can be predicted through a number of theoretical and numerical methods, ranging from quasi-exact discrete dipole models to full-field simulation with finite element or finite-difference time-domain methods. While these techniques can solve many scattering problems to arbitrary accuracy, they require fine knowledge of the structure of interest for their results to be applicable. The most ambitious model-based parameter retrieval would be to attempt inversion of the scattering problem. While in the simplest of cases, it may be possible to invert scattering problems analytically by working out the parameter dependence of certain far-field information channels, this route of direct inversion is generally infeasible to retrieve arbitrary parameters for realistic systems. The difficulty stems from the nonseparable dependence of observables on various parameters, including possible quantities of interest, caused by two aspects of the physics at play. In the dipole scatterer at hand, coupling between different induced dipoles depends nonlinearly on relative positions and drive frequency. Moreover, optical experiments have much more convenient access to field intensity than to the full complex field, which precludes direct numerical back-propagation of the far-field data to reconstruct the light source.

Without a direct inversion approach, parameter retrieval would have to be performed through some combination of tabulating forward modeling results and matching to measured data. This approach would be tantamount to building a library of model results instead of measured reference data. In large-scale applications, like CMOS manufacturing fabrication processes, that are very well characterized, such a priori predictive approaches may prove valuable. Unfortunately, for most other branches of nanofabrication to realize scattering structures, the predictions of models are generally not robust to the fabrication imperfections that occur in actual devices. We argue, based on the present work, to instead make use of real-world calibration of scattering patterns without any assistance from modeling. This has the benefit that it only requires experimental conditions and device properties to be unchanged between the moment of building up the library for a structure and use of the structure for metrology. Indeed, as our experimental realization (reported below) shows it is entirely possible to build up a library of scattering patterns versus some known parameter for a single device without knowing or modeling the precise device geometry and without needing to account for any distortions of the far-field patterns downstream in the optical measurement system. Given sufficiently low noise and an appropriate comparison algorithm, the library entry with the same parameter values

will provide an excellent match to the experimental result without recourse to modeling.

Finally, we note that the concept of a library, and subsequent retrieval of parameters allows for other solutions than PCA-based techniques. Recently, several groups have addressed related challenges through machine learning, successfully retrieving parameters with subdiffractive precision as good as $\lambda/25$ for optical wavelength λ.[41,42] For such demonstrations, the number of distinguishable parameter values is typically orders of magnitude smaller than the size of the "training set", that is, the size of the calibration library that is required. In an additional drawback, it is often difficult to interpret how the neural network performs its function and whether it is robust to minor changes in parameters, regularization being one of the oldest[43] and toughest[44] problems in machine learning. Instead, using a calibration-based, transparent method, we precisely retrieve parameter values with small reference libraries and additionally gain insight into the structure of the reference data.

■ EXPERIMENTAL REALIZATION

We demonstrate the proposed imaging-free super-resolution technique experimentally, by retrieving the position of a point-like source of light with respect to a known scattering nanostructure. We induce point-like light emission by focusing a high-energy electron beam (30 keV) on a substrate in a scanning electron microscope. Where the electrons cross the vacuum/gold interface, the rapid change in electric field dynamically polarizes the material, causing light emission through cathodoluminescence.[45,46] For optical purposes, this light source can be modeled as a radiating out-of-plane point dipole at the interface, its apparent size being set by the focal spot of the electron beam.[47,48] We collect the light emitted in this process using a parabolic mirror of acceptance angle 1.47 sr and project it onto a camera, revealing the radiation pattern as radiated intensity versus emission angle.[49,50] We filter the light down to a band around $\lambda = 500$ nm to avoid washing out of features in radiation patterns. Figure 4a schematically shows the key parts of our angle-resolved cathodoluminescence setup. As scattering nanostructure we use a bullseye antenna, a type of structure well-known for its strong beaming[51] and widely used to control light emission from nanoscale sources.[33,52−56] The antenna, shown in Figure 4b, is fabricated by FIB milling of monocrystalline gold and consists of a 1.2 μm plateau surrounded by 8 concentric grooves, 600 nm in width and around 100 nm in depth, separated by ridges 600 nm in width. With a point-like light source on the symmetry axis of the bullseye, the radiation pattern will likewise be cylindrically symmetric. As the light source moves away from the symmetry axis, the radiation pattern shifts as propagation delay changes the relative phase between scattering sites.

We capture such radiation patterns and transform them to momentum space,[49] leading to images of radiant flux versus emission direction like those shown in Figure 4c,d, taken at positions 500 nm northwest (Figure 4c) and southeast (Figure 4d) of the bullseye antenna center. The main feature in both patterns is a ring-like structure around the center that shifts its intensity maximum to different angles as electron beam position changes. This feature is attributed to beaming and matches literature reports on similar structures.[50] Blind spots caused by the finite extent of the mirror and a hole through which the electron beam reaches the sample do not hinder observation of the position-dependent features.
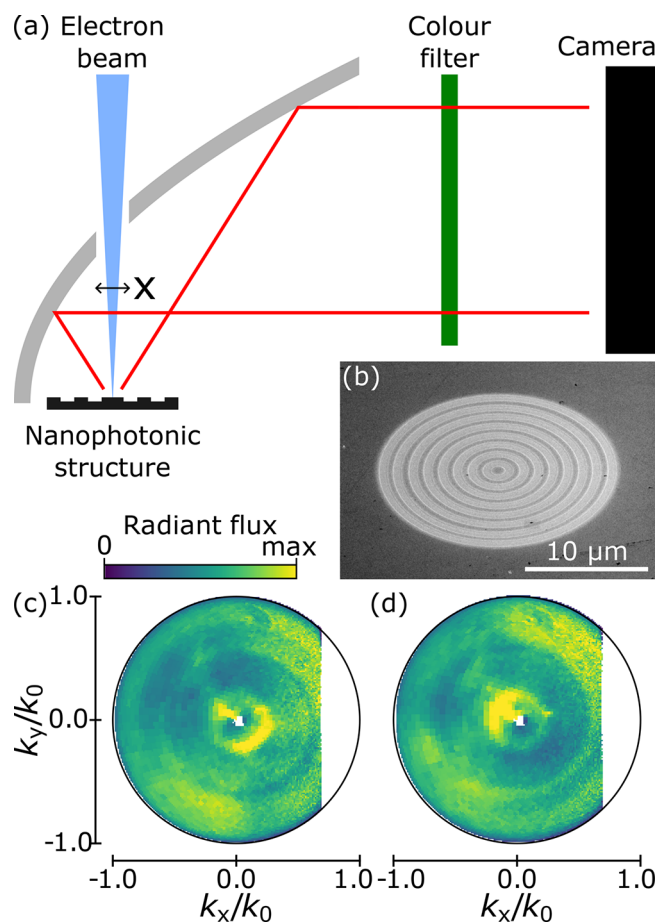

Figure 4. Experimental realization of a light source moving with respect to a nanophotonic structure. (a) Layout of the main parts of the cathodoluminescence setup used in these experiments. An electron beam is focused onto a bullseye antenna and induces light emission. A parabolic mirror, with its focal point on the antenna, captures this light and directs it through a color filter to a camera. (b) The bullseye antenna used in the measurements presented here. (c) Radiation pattern constructed from camera image with light source 500 nm ($=\lambda$) northwest of center on the central plateau of the bullseye antenna. Wavevectors not captured by the mirror are masked in white. (d) Like (c), but with light source 500 nm southeast of center.

We now compose a reference data set for 8×8 electron beam positions in a grid with 100 nm ($\lambda/5$) steps. This grid is situated around the center of the central plateau of the bullseye antenna and covers most of it; Figure 4c,d corresponds to the radiation patterns at two opposite corners. We normalize the data set as before and take its SVD in order to apply our localization algorithm. Figure 5a shows part of the SVD constructed for this data set. Like for the synthetic data, the first basis element is a largely position-independent background. Subsequent elements again show smooth features both in basis elements and in position dependence. For instance, one may recognize beaming along both diagonals in the third and fourth elements, which occurs for light source positions off-center along the appropriate diagonal.

As for the synthetic data, we can compare sample measurements with the library to find position estimates. To this end, we take sample measurements at positions identical to reference positions, within experimental accuracy. Projecting individual measurements onto the reference library reveals a
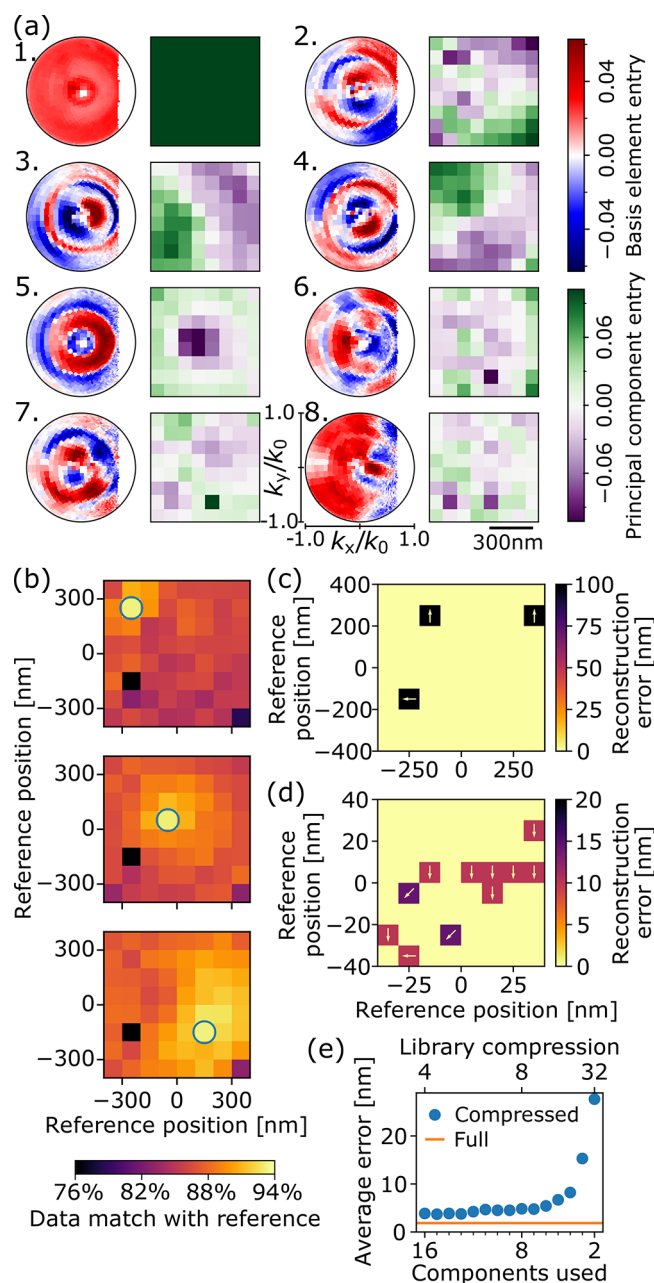
Figure 5. Parameter retrieval with an experimental reference library. (a) SVD for an experimental reference data set, shown as in Figure 2d. The central plateau of the bullseye antenna is slightly wider than the diagonal of the principal component maps. (b) Comparing new data with the reference library for three positions, indicated by circles. (c) Position estimates for test data based on localization algorithm vs actual position. Color scale indicates error between best estimate and known position. Where estimates were incorrect, arrows indicate the direction of the error. Data shown are for a grid with 100 nm steps. (d) Like (c), but 10 nm steps. (e) Average error vs library compression.

identified correctly (94% of positions match). To explore the position retrieval precision, we repeat calibration, measurement, and analysis on an 8 × 8 grid with much smaller position steps of 10 nm. As seen in Figure 5d, most positions (81%) are still identified correctly. The average position retrieval error is below 5 nm ($\lambda/100$). Where positions were not retrieved correctly, we see a clear correlation in error directions (southward). This is reminiscent of the behavior seen in our theoretical demonstration when using a displaced sampling grid (Figure 3e), suggesting that errors may be dominated by a small systematic drift in bullseye position between measurement of calibration and sample data. Localization may thus be more accurate than our technical implementation can show.

So far, the full library has been used to estimate light source position. As discussed previously, most spatial information is contained in those few basis elements with largest principal components. Disregarding the low-weight elements in the optimal basis allows us to compress the library: if N_{used} out of N_{tot} basis elements are used for position retrieval, we reach library compression of a factor N_{tot}/N_{used}. We explore how this compression affects localization precision. For the set of measurements on the 10 nm grid, half the optimal basis may be discarded without any loss in localization performance. Figure 5e shows how average error varies as a function of the number of basis elements used. Average error grows slowly as the library is compressed until just a few basis elements are left, as we expected from the large weight of the most important elements. In fact, using just four basis elements, for library compression by a factor 16, average localization error stays below 10 nm. This means that the calibration data can be stored in a highly efficient way, but also shows how SVD has identified the most vital features of the radiation patterns, speaking for the robustness of the localization technique.

To investigate the contribution of the nanophotonic structure to the success of the localization experiment, we compare the previously discussed experimental results with measurements taken on plain gold. Radiation will be emitted even in the absence of surface structuring, with a radiation pattern that is of course expected to be entirely independent of where the electron beam excites the surface. Thus, source localization should be strictly impossible in absence of a nanophotonic scattering structure. In practice, in our setup, captured radiation patterns will vary slightly as the electron beam is scanned around the mirror focus, owing to off-axis aberrations of the parabolic collection mirror. In Figure 6a, we show the SVD for a data set for 5 × 5 electron beam positions in a grid with 200 nm steps on plain gold. In contrast with the data presented in Figure 5a, there is fairly little spatial structure in either the basis elements or the principal components after the background. What little structure can still be seen in the third and fourth basis elements is likely due to mirror aberrations, due to which some position information can still be extracted. The drastic loss in basis element structure from removal of the antenna indicates that the plain gold radiation patterns do not encode an electron beam position in any clear features.

The effect of the nanophotonic structure is seen most clearly in the singular values. In Figure 6b we compare the plain gold data set with a data set taken with the same experimental parameters on a bullseye antenna. The first singular value, reflecting background signal, is identical for the two cases. Subsequent singular values, however, are lower and drop off much more quickly for plain gold than with bullseye antenna.
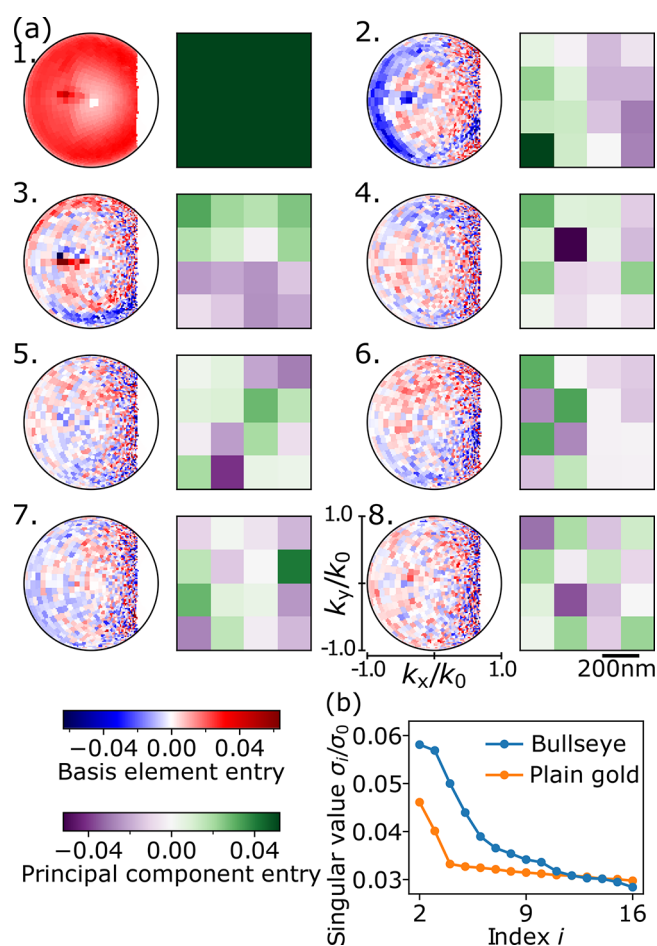
projection match landscape as before. As seen in Figure 5b, these landscapes typically peak at the correct sample positions, indicated with circles, as in the numerical example before. Comparing best estimates with known positions gives a vectorial localization error. Figure 5c shows a map of localization error versus position, where colors indicate the magnitude of errors and arrows indicate in which direction the error was made, if any. We see that almost all positions were

Figure 6. Experimental data without nanostructure. (a) SVD of radiation patterns for a grid of electron beam positions on plain gold, as shown in Figure 2d. (b) Comparing singular values between reference data sets on a nanostructure and on plain gold.

bullseye antenna, with few-nanometer, $\lambda/100$, precision, deeply below the diffraction limit. These results are achieved at signal-to-noise ratios that are not particularly demanding to reach, comparable with those commonly encountered in, for instance, single molecule microscopy and single nanoparticle darkfield scatterometry. We require a bare minimum of calibration images, one library entry per source position, in contrast with the vast quantities of calibration data used in machine learning-based methods. Localization is shown to work well over ranges from hundreds to tens of nanometers, with precision possibly limited only by the accuracy and tolerances of the experimental setup. The PCA-based technique provides a number of handles that provide insight into the pattern recognition upon which it operates, particularly direct visualization of the principal components of calibration data and of the projection match for different reference positions. Our numerical and experimental demonstrations both show smooth optimal basis elements and principal components, implying a degree of robustness of localization success to experimental drifts and noise. For our experimental demonstration, comparison between nanophotonically mediated reference data and those generated by a light source on plain gold reveals how localization is facilitated by the complexity introduced to the radiation patterns by the nanophotonic structure.

Unlike common imaging techniques, our method does not rely on a sharp PSF, but rather uses partial information about the sample to directly invert measured data to a given parameter. This means we cannot define an intrinsic resolution for our method based on the PSF width. Though we have shown deeply subdiffractive localization precision, this precision will ultimately depend on the interplay between signal-to-noise ratio and the length scale over which measured signals, like radiation patterns, change. It is interesting to consider how the underlying physics may be used to tune this length scale. We know that variations in the size of structures affect radiation patterns through their structure factor, which varies over length scales comparable with the wavelength of the light used. Hybridization between nanophotonic scatterers, on the other hand, leads to strong changes in spectral response and radiation patterns when scattering sites move at separations of a small fraction of the wavelength. Careful engineering of the interplay between these effects, and so, of the optical modes of the overall structure may allow future work to tailor transducers for improved localization range and precision.

We have shown examples of retrieval of light source position from radiation patterns, but we believe the method itself can be applied much more generally. For instance, we expect the same approach to be able to retrieve arbitrary parameters that affect far-field information channels, including orientation and relative scattering strength between sites, spectral properties, and absence or presence of sample features. Initial theoretical results suggest that retrieval of the positions of multiple coherent light sources is feasible; further exploration may be able to quantify these results and extend them to incoherent sources and imaging-like problems. The method also does not necessarily depend on radiation patterns, and we believe that parameter retrieval may be performed based on such information channels as scattered optical frequency spectrum or, indeed, based on real-space images, possibly with whatever sort of optical distortion, as in the problems studied in the field of imaging through complex media. Vastly reduced angular information may prove sufficient for parameter retrieval in low-

Both sets of singular values eventually tend to the noise level, but the greater number of large singular values indicates the additional position information encoded in the radiation patterns by the nanophotonic structure. At this large step size, it is just barely possible to reconstruct an electron beam position on plain gold, in contrast with very reliable reconstruction on the bullseye antenna. What little spatial information remains in the transducer-free experiment may be attributed to aberrations, which could be further reduced by experimental tweaks, but are already minute compared to the wealth of spatial information provided by the bullseye antenna. This shows that scattering by the nanophotonic structure is essential to our technique.

■ CONCLUSIONS AND DISCUSSION

We have proposed a library-based approach to extract nanoscale spatial information about structures from far-field radiation patterns, that is, without the use of a real-space imaging setup. We explored the proposed imaging-free localization method theoretically, demonstrating that principal component analysis of radiation patterns can produce libraries that efficiently encode nanoscale parameters of scattering systems. In our experimental demonstration, we have shown that the proposed method is able to retrieve a light source position relative to a nanophotonic system, in the form of a

dimensional problems, or conversely, inclusion of phase or polarization information may allow more precise and more efficient parameter retrieval. For problems where calibration with experimental data is infeasible, the method can be adapted to use synthetic reference data generated by a physical model. The method is specifically intended to be applicable to architectures other than the cathodoluminescence setup used in our experimental demonstration. A carefully characterized collection of structures with randomly deposited luminescent particles may serve as the reference set for retrieval of particle position or orientation on new structures. Another approach is to exploit the analogy between the cathodoluminescence-induced light source, which is like a vertically oriented dipole source, and structures of interest well described by out-of-plane dipole moments. This would allow building a library using cathodoluminescence and using the observed radiation patterns to retrieve the precise position of other vertically oriented emitters. While transition radiation in CL provides information for vertically oriented dipoles only, one can also envision building libraries for in-plane or random dipole orientations using samples with deliberately included emitters at shallow depths (e.g., quantum wells, phosphor films). Given the generality of our method across parameters and architectures, we foresee a wide range of applications in nanoscale metrology.

METHODS

Model. Our scattering example system consists of a point source of light moving in a plane $\lambda/4$ below a linear array of four scattering sites spaced $\lambda/4$ apart. The array particles are strong scatterers with a $Q = 10$ resonance around the drive frequency, as might be found for silver nanoparticles around 100 nm in diameter and resonant at visible wavelengths.[24] We use a dipolar drive field oriented along the long axis of the array as a light source. Discrete dipole calculations were made using custom code implementing the Green's function of a dipole and coupling matrix inversion in Python. The SVD algorithm is deterministic and results should be identical between the many available implementations; we use the implementation in the Python NumPy library.

Plasmon Antenna. The bullseye antenna was fabricated by removing excess material in Czochralski-grown ⟨111⟩ single-crystalline gold. Focused ion beam milling was performed in a FEI Helios NanoLab dual SEM/FIB system with a 9.7 pA beam of 30 keV Ga+ ions over 100 rounds with pixel dwell time 10 μs at pixel pitch 7.5 nm.

Cathodoluminescence Setup. Cathodoluminescence measurements were taken in a Thermo Fisher 650 Quanta SEM system and analyzed in a Delmic SPARC system. Radiation patterns were generated with a 4 nA electron beam at an energy of 30 keV, collected with an aluminum mirror of acceptance angle 1.47π sr, filtered down to a 40 nm band around $\lambda = 500$ nm, and integrated for 30 s on a back-illuminated CCD camera. A full set of 8×8 measurements thus took 32 min of integration. To limit the effects of sample stage drift, drift correction was performed every second during integration by taking an SEM image of a known region and automatically repositioning based on observed position error. Background correction was performed by subtracting radiation patterns collected with blanked electron beam.

AUTHOR INFORMATION

Corresponding Author

A. Femius Koenderink − *Center for Nanophotonics, AMOLF, 1098XG Amsterdam, The Netherlands;* orcid.org/0000-0003-1617-5748; Email: f.koenderink@amolf.nl

Authors

Robin D. Buijs − *Center for Nanophotonics, AMOLF, 1098XG Amsterdam, The Netherlands*

Nick J. Schilder − *Center for Nanophotonics, AMOLF, 1098XG Amsterdam, The Netherlands;* orcid.org/0000-0002-7549-5146

Tom A. W. Wolterink − *Center for Nanophotonics, AMOLF, 1098XG Amsterdam, The Netherlands;* orcid.org/0000-0002-3591-8044

Giampiero Gerini − *Optics Department, Netherlands Organization for Applied Scientific Research (TNO), 2628CK Delft, The Netherlands; Department of Electrical Engineering, Technische Universiteit Eindhoven (TU/e), 5600MB Eindhoven, The Netherlands*

Ewold Verhagen − *Center for Nanophotonics, AMOLF, 1098XG Amsterdam, The Netherlands;* orcid.org/0000-0002-0276-8430

Complete contact information is available at:
https://pubs.acs.org/10.1021/acsphotonics.0c01350

Notes

The authors declare no competing financial interest.

REFERENCES

(1) Abbe, E. Beiträge zur Theorie des Mikroskops und der mikroskopischen Wahrnehmung. *Arch. Mikrosk. Anat.* **1873**, *9*, 413−468.

(2) Huszka, G.; Gijs, M. A. Super-resolution optical imaging: A comparison. *Micro- Nano Eng.* **2019**, *2*, 7−28.

(3) Pujals, S.; Feiner-Gracia, N.; Delcanale, P.; Voets, I.; Albertazzi, L. Super-resolution microscopy as a powerful tool to study complex synthetic materials. *Nat. Rev. Chem.* **2019**, *3*, 68−84.

(4) Gåsvik, K. J. *Optical Metrology*; Wiley, 2002.

(5) Yoshizawa, T., Ed. *Handbook of Optical Metrology*; CRC Press, 2017.

(6) Klar, T. A.; Hell, S. W. Subdiffraction resolution in far-field fluorescence microscopy. *Opt. Lett.* **1999**, *24*, 954.

(7) Betzig, E.; Patterson, G. H.; Sougrat, R.; Lindwasser, O. W.; Olenych, S.; Bonifacino, J. S.; Davidson, M. W.; Lippincott-Schwartz, J.; Hess, H. F. Imaging Intracellular Fluorescent Proteins at Nanometer Resolution. *Science* **2006**, *313*, 1642−1645.

(8) Thorley, J. A.; Pike, J.; Rappoport, J. Z. *Fluorescence Microscopy*; Elsevier, 2014; pp 199−212.

(9) Pohl, D. W.; Denk, W.; Lanz, M. Optical stethoscopy: Image recording with resolution $\lambda/20$. *Appl. Phys. Lett.* **1984**, *44*, 651−653.

(10) Taubner, T.; Keilmann, F.; Hillenbrand, R. Nanoscale-resolved subsurface imaging by scattering-type near-field optical microscopy. *Opt. Express* **2005**, *13*, 8893.

(11) Lereu, A.; Passian, A.; Dumas, P. Near field optical microscopy: a brief review. *Int. J. Nanotechnol.* **2012**, *9*, 488.

(12) Kolenov, D.; Pereira, S. F. Machine learning techniques applied for the detection of nanoparticles on surfaces using coherent Fourier scatterometry. *Opt. Express* **2020**, *28*, 19163.

(13) Bouchet, D.; Carminati, R.; Mosk, A. P. Influence of the Local Scattering Environment on the Localization Precision of Single Particles. *Phys. Rev. Lett.* **2020**, *124*, 133903.

(14) Neugebauer, M.; Woźniak, P.; Bag, A.; Leuchs, G.; Banzer, P. Polarization-controlled directional scattering for nanoscopic position sensing. *Nat. Commun.* **2016**, *7*, 11286.

(15) Shang, W.; Xiao, F.; Zhu, W.; Han, L.; Premaratne, M.; Mei, T.; Zhao, J. Unidirectional scattering exploited transverse displacement sensor with tunable measuring range. *Opt. Express* **2019**, *27*, 4944.

(16) Bag, A.; Neugebauer, M.; Mick, U.; Christiansen, S.; Schulz, S. A.; Banzer, P. Towards fully integrated photonic displacement sensors. *Nat. Commun.* **2020**, *11*, 2915.

(17) Rochon, P.; Bissonnette, D. Lensless imaging due to back-scattering. *Nature* **1990**, *348*, 708−710.

(18) Zhang, T.; Godavarthi, C.; Chaumet, P. C.; Maire, G.; Giovannini, H.; Talneau, A.; Allain, M.; Belkebir, K.; Sentenac, A. Far-field diffraction microscopy at $\lambda/10$ resolution. *Optica* **2016**, *3*, 609.

(19) Unger, K. D.; Chaumet, P. C.; Maire, G.; Sentenac, A.; Belkebir, K. Versatile inversion tool for phaseless optical diffraction tomography. *J. Opt. Soc. Am. A* **2019**, *36*, C1.

(20) Vellekoop, I. M.; Mosk, A. P. Focusing coherent light through opaque strongly scattering media. *Opt. Lett.* **2007**, *32*, 2309.

(21) Harm, W.; Roider, C.; Jesacher, A.; Bernet, S.; Ritsch-Marte, M. Lensless imaging through thin diffusive media. *Opt. Express* **2014**, *22*, 22146.

(22) Horisaki, R.; Okamoto, Y.; Tanida, J. Single-shot noninvasive three-dimensional imaging through scattering media. *Opt. Lett.* **2019**, *44*, 4032.

(23) Kim, D.; Englund, D. R. Quantum reference beacon−guided superresolution optical focusing in complex media. *Science* **2019**, *363*, 528−531.

(24) Link, S.; El-Sayed, M. A. Size and Temperature Dependence of the Plasmon Absorption of Colloidal Gold Nanoparticles. *J. Phys. Chem. B* **1999**, *103*, 4212−4217.

(25) Zhao, L.; Kelly, K. L.; Schatz, G. C. The Extinction Spectra of Silver Nanoparticle Arrays: Influence of Array Structure on Plasmon Resonance Wavelength and Width. *J. Phys. Chem. B* **2003**, *107*, 7343−7350.

(26) Weber, W. H.; Ford, G. W. Propagation of optical excitations by dipolar interactions in metal nanoparticle chains. *Phys. Rev. B: Condens. Matter Mater. Phys.* **2004**, *70*, 125429.

(27) Yurkin, M.; Hoekstra, A. The discrete dipole approximation: An overview and recent developments. *J. Quant. Spectrosc. Radiat. Transfer* **2007**, *106*, 558−589.

(28) Chaumet, P. C.; Zhang, T.; Sentenac, A. Fast far-field calculation in the discrete dipole approximation. *J. Quant. Spectrosc. Radiat. Transfer* **2015**, *165*, 88−92.

(29) Novotny, L.; Hecht, B. *Principles of Nano-Optics*; Cambridge University Press, 2006.

(30) García de Abajo, F. J. Colloquium: Light scattering by particle and hole arrays. *Rev. Mod. Phys.* **2007**, *79*, 1267−1290.

(31) Lieb, M. A.; Zavislan, J. M.; Novotny, L. Single-molecule orientations determined by direct emission pattern imaging. *J. Opt. Soc. Am. B* **2004**, *21*, 1210.

(32) Patra, D.; Gregor, I.; Enderlein, J.; Sauer, M. Defocused imaging of quantum-dot angular distribution of radiation. *Appl. Phys. Lett.* **2005**, *87*, 101103.

(33) Osorio, C. I.; Mohtashami, A.; Koenderink, A. F. K-space polarimetry of bullseye plasmon antennas. *Sci. Rep.* **2015**, *5*, 9966.

(34) Jolliffe, I. T.; Cadima, J. Principal component analysis: a review and recent developments. *Philos. Trans. R. Soc., A* **2016**, *374*, 20150202.

(35) Jesse, S.; Kalinin, S. V. Principal component and spatial correlation analysis of spectroscopic-imaging data in scanning probe microscopy. *Nanotechnology* **2009**, *20*, 085714.

(36) Melati, D.; Grinberg, Y.; Dezfouli, M. K.; Janz, S.; Cheben, P.; Schmid, J. H.; Sánchez-Postigo, A.; Xu, D.-X. Mapping the global design space of nanophotonic components using machine learning pattern recognition. *Nat. Commun.* **2019**, *10*, 4775.

(37) Jolliffe, I. T. *Principal Component Analysis*; Springer-Verlag, 2002.

(38) Koenderink, A. F. Plasmon Nanoparticle Array Waveguides for Single Photon and Single Plasmon Sources. *Nano Lett.* **2009**, *9*, 4228−4233.

(39) Li, J.; Salandrino, A.; Engheta, N. Shaping light beams in the nanometer scale: A Yagi-Uda nanoantenna in the optical domain. *Phys. Rev. B: Condens. Matter Mater. Phys.* **2007**, *76*, 245403.

(40) Coenen, T.; Vesseur, E. J. R.; Polman, A.; Koenderink, A. F. Directional Emission from Plasmonic Yagi−Uda Antennas Probed by Angle-Resolved Cathodoluminescence Spectroscopy. *Nano Lett.* **2011**, *11*, 3779−3784.

(41) Pu, T.; Ou, J. Y.; Papasimakis, N.; Zheludev, N. I. Label-free deeply subwavelength optical microscopy. *Appl. Phys. Lett.* **2020**, *116*, 131105.

(42) Ghosh, A.; Roth, D. J.; Nicholls, L. H.; Wardley, W. P.; Zayats, A. V.; Podolskiy, V. A. Machine learning-based diffractive imaging with subwavelength resolution. *CLEO: QELS Fundamental Science* **2020**, FW3B.7.

(43) Baum, E. B.; Haussler, D. What Size Net Gives Valid Generalization? *Neural Computation* **1989**, *1*, 151−160.

(44) Goodfellow, I.; Bengio, Y.; Courville, A. *Deep Learning*; MIT Press, 2016, http://www.deeplearningbook.org.

(45) Yamamoto, N.; Araya, K.; Toda, A.; Sugiyama, H. Light emission from surfaces, thin films and particles induced by high-energy electron beam. *Surf. Interface Anal.* **2001**, *31*, 79−86.

(46) van Wijngaarden, J. T.; Verhagen, E.; Polman, A.; Ross, C. E.; Lezec, H. J.; Atwater, H. A. Direct imaging of propagation and damping of near-resonance surface plasmon polaritons using cathodoluminescence spectroscopy. *Appl. Phys. Lett.* **2006**, *88*, 221111.

(47) García de Abajo, F. J. Optical excitations in electron microscopy. *Rev. Mod. Phys.* **2010**, *82*, 209−275.

(48) Kuttge, M.; Vesseur, E. J. R.; Koenderink, A. F.; Lezec, H. J.; Atwater, H. A.; de Abajo, F. J. G.; Polman, A. Local density of states, spectrum, and far-field interference of surface plasmon polaritons probed by cathodoluminescence. *Phys. Rev. B: Condens. Matter Mater. Phys.* **2009**, *79*, 113405.

(49) Coenen, T.; Vesseur, E. J. R.; Polman, A. Angle-resolved cathodoluminescence spectroscopy. *Appl. Phys. Lett.* **2011**, *99*, 143103.

(50) Osorio, C. I.; Coenen, T.; Brenny, B. J. M.; Polman, A.; Koenderink, A. F. Angle-Resolved Cathodoluminescence Imaging Polarimetry. *ACS Photonics* **2016**, *3*, 147−154.

(51) Martín-Moreno, L.; García-Vidal, F. J.; Lezec, H. J.; Degiron, A.; Ebbesen, T. W. Theory of Highly Directional Emission from a Single Subwavelength Aperture Surrounded by Surface Corrugations. *Phys. Rev. Lett.* **2003**, *90*, 167401.

(52) Lezec, H. J. Beaming Light from a Subwavelength Aperture. *Science* **2002**, *297*, 820−822.

(53) Aouani, H.; Mahboub, O.; Bonod, N.; Devaux, E.; Popov, E.; Rigneault, H.; Ebbesen, T. W.; Wenger, J. Bright Unidirectional Fluorescence Emission of Molecules in a Nanoaperture with Plasmonic Corrugations. *Nano Lett.* **2011**, *11*, 637−644.

(54) Gorodetski, Y.; Lombard, E.; Drezet, A.; Genet, C.; Ebbesen, T. W. A perfect plasmonic quarter-wave plate. *Appl. Phys. Lett.* **2012**, *101*, 201103.

(55) Crick, C. R.; Albella, P.; Ng, B.; Ivanov, A. P.; Roschuk, T.; Cecchini, M. P.; Bresme, F.; Maier, S. A.; Edel, J. B. Precise Attoliter Temperature Control of Nanopore Sensors Using a Nanoplasmonic Bullseye. *Nano Lett.* **2015**, *15*, 553−559.

(56) Coenen, T.; Polman, A. Energy-Momentum Cathodoluminescence Imaging of Anisotropic Directionality in Elliptical Aluminum Plasmonic Bullseye Antennas. *ACS Photonics* **2019**, *6*, 573−580.